Two-photon microscopy of cortical NADH fluorescence intensity changes: correcting contamination from the hemodynamic response

Edward Baraghis
Anna Devor
Qianqian Fang
Vivek J. Srinivasan
Weicheng Wu
Frédéric Lesage
Cenk Ayata
Karl A. Kasischke
David A. Boas
Sava Sakadžić

Two-photon microscopy of cortical NADH fluorescence intensity changes: correcting contamination from the hemodynamic response

Edward Baraghis,[a,b] **Anna Devor,**[a,c] **Qianqian Fang,**[a] **Vivek J. Srinivasan,**[a] **Weicheng Wu,**[a] **Frédéric Lesage,**[b] **Cenk Ayata,**[d,e]
Karl A. Kasischke,[f] **David A. Boas,**[a] **and Sava Sakadžić**[a]
[a]Harvard Medical School, Massachusetts General Hospital, Department of Radiology, 149 13th Street,
Charlestown, Massachusetts 02129
[b]École Polytechnique de Montréal, Département de génie électrique, Montreal, Canada H3C 3A7
[c]University of California, Departments of Neurosciences and Radiology, San Diego, California 92093
[d]Harvard Medical School, Massachusetts General Hospital, Department of Radiology, Neurovascular Research
Laboratory, Charlestown, Massachusetts 02129
[e]Massachusetts General Hospital, Department of Neurology, Stroke Service and Neuroscience Intensive Care Unit,
Boston, Massachusetts 02114
[f]University of Rochester Medical Center, Department of Neurology, Center for Neural Development and Disease,
Rochester, New York 14642

Abstract. Quantification of nicotinamide adenine dinucleotide (NADH) changes during functional brain activation and pathological conditions provides critical insight into brain metabolism. Of the different imaging modalities, two-photon laser scanning microscopy (TPLSM) is becoming an important tool for cellular-resolution measurements of NADH changes associated with cellular metabolic changes. However, NADH fluorescence emission is strongly absorbed by hemoglobin. As a result, *in vivo* measurements are significantly affected by the hemodynamics associated with physiological and pathophysiological manipulations. We model NADH fluorescence excitation and emission in TPLSM imaging based on precise maps of cerebral microvasculature. The effects of hemoglobin optical absorption and optical scattering from red blood cells, changes in blood volume and hemoglobin oxygen saturation, vessel size, and location with respect to imaging location are explored. A simple technique for correcting the measured NADH fluorescence intensity changes is provided, with the utilization of a parallel measurement of a physiologically inert fluorophore. The model is applied to TPLSM measurements of NADH fluorescence intensity changes in rat somatosensory cortex during mild hypoxia and hyperoxia. The general approach of the correction algorithm can be extended to other TPLSM measurements, where changes in the optical properties of the tissue confound physiological measurements, such as the detection of calcium dynamics. © *2011 Society of Photo-Optical Instrumentation Engineers (SPIE)*. [DOI: 10.1117/1.3633339]

Keywords: nicotinamide adenine dinucleotide fluorescence; two-photon laser scanning microscopy; brain imaging; correction algorithms; Monte Carlo simulations; optical scattering; hemoglobin absorption.

Paper 11200R received Apr. 20, 2011; revised manuscript received Jul. 20, 2011; accepted for publication Aug. 12, 2011; published online Oct. 3, 2011.

1 Introduction

The intracellular coenzyme nicotinamide adenine dinucleotide (NADH) is one of the key cellular metabolic markers.[1] The NADH autofluorescence has been utilized extensively in the past for noninvasive assessment of tissue metabolic state and oxygenation.[2,3] In addition to linear excitation of NADH fluorescence, a relatively small but sufficient two-photon absorption cross section exists in the near-infrared spectrum from 700 to 750 nm,[4] which allows two-photon laser scanning microscopy (TPLSM) imaging of NADH fluorescence.[4–9] The advantages of TPLSM imaging for *in vivo*, depth-resolved high-resolution imaging in highly scattering brain tissue make TPLSM imaging of NADH fluorescence very attractive for investigating brain metabolism. However, changes in brain activity resulting from either functional stimulation or various pathological condi-

tions are typically coupled with strong hemodynamic responses, which alter the optical properties of the tissue and subsequently interfere with the measured NADH fluorescence signal.[2] The NADH fluorescence emission spectrum[1] has a maximum at 450–460 nm and is strongly absorbed by hemoglobin—the main optical absorber in the cortex in the visible and near-infrared regions of the spectrum. In addition, changes in blood volume affect the optical scattering of the excitation light, which has a profound effect on nonlinear two-photon excitation. At excitation wavelengths typically used in TPLSM imaging of NADH fluorescence (700–740 nm), the optical scattering coefficient of blood ($> 100\ \text{mm}^{-1}$)[10–13] is an order of magnitude larger than the scattering coefficient in the cortical tissue ($\sim 10\ \text{mm}^{-1}$),[14–17] and the significant decrease in detected fluorescence is evident underneath the blood vessels in TPLSM brain images.[18] Therefore, TPLSM imaging of NADH fluorescence changes could be affected by the blood volume and oxygenation changes starting at imaging depths of only a few tens of microns. Further

Address all correspondence to: Sava Sakadžić, Harvard Medical School, Massachusetts General Hospital, Department of Radiology, 149 13th Street, Room 2301, Charleston, Massachusetts 02129. Tel: 617-726-9338; E-mail: sava@nmr.mgh.harvard.edu.

progress in utilizing TPLSM imaging of NADH fluorescence for understanding brain metabolism and oxygenation is dependent on our better understanding of the confounding effect of the hemodynamic response on the measured NADH signal, especially in the case of functional brain activation with relatively small expected NADH signal changes.

Here, we utilized realistic three-dimensional (3-D) microvascular anatomical networks of cortical microvasculature obtained by *in vivo* TPLSM imaging. By using ray-tracing algorithms and Monte Carlo modeling of light propagation in the scattering media, we explored the influence of blood vessel size, imaging depth, and lateral distance from the microvasculature, imaging objective numerical aperture, and blood volume and oxygenation changes on measured changes of NADH fluorescence intensity. We provide detailed maps of NADH signal measurement error due to blood volume changes for various imaging depths, vessel diameters, and lateral measurement distances from the vessels. Finally, we explored the possibility of correcting the measured NADH fluorescence signal changes by simultaneously measuring the fluorescence intensity changes of an additional physiologically inert fluorophore. Although the microscopic forward modeling can be directly applied in individual measurement configurations to correct for the influence of the hemodynamic response on the NADH signal, our study suggests that a simple empirical correction formula can be applied in many cases without detailed knowledge of the microvascular structure. We present examples of this correction formula applied to measurements of NADH fluorescence intensity changes in rat cortices during mild hypoxia and hyperoxia.

2 Methods

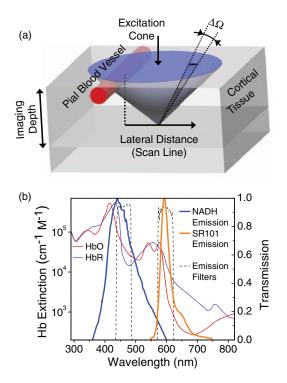### 2.1 Two-Photon Laser Scanning Microscopy Setup

Imaging was performed using a commercial two-photon laser scanning microscope (Ultima, Prairie Technologies, Inc., Middleton, Wisconsin). Excitation was provided in the epi-illumination configuration. Scanning of a single optical beam in the XY plane, perpendicular to the optical Z-axis, was performed by a pair of conventional nonresonant galvanometer-based scanners. The fine positioning of the microscope objective along the optical axis was controlled by a motorized stage. The emission from the sample was reflected by a high-pass dichroic mirror positioned close to the back aperture of the objective and detected by a four-channel detector. The emission light inside the four-channel detector was split by the dichroic mirror into two arms, each containing a filter cube and a pair of photomultiplier tubes (PMTs) operating in analog mode. The transmission windows of emission filters in front of the detectors were 460 ± 25, 525 ± 25, 595 ± 25, and 660 ± 20 nm. The PMTs output current was amplified and the signal digitized by a 12-bit analog-to-digital converter (ADC) at 2.5×10^6 samples/s. The intensity of a single pixel in the image frame was calculated as a sum of all the ADC samples obtained during the pixel dwell time. Imaging was performed using an Olympus XLUMPLFL 20X objective [2-mm working distance, water immersion, numerical aperture (NA) = 0.95]. The excitation beam at 740 nm was generated by a femtosecond laser (Mai-Tai, Spectra-Physics, Irvine, California). The optical power on the sample was controlled by an electro-optic modulator (Conoptics Inc., Danbury, Connecti-

cut), and the excitation beam width ($1/e^2$) at the back aperture of the objective was 9.1 mm.

2.2 Animal Preparation and Two-Photon Laser Scanning Microscopy Imaging of NADH Fluorescence During Hypoxia and Hyperoxia in Rats

Male Sprague Dawley rats (250–320 g, six animals, 17 experimental trials) were anesthetized with isoflurane (1–2% in a mixture of O_2 and N_2O) under constant temperature (37 °C). A catheter was inserted in the femoral artery to monitor blood pressure (80–110 mmHg), blood gases (pO$_2$, 100–130 mmHg, and pCO$_2$, 34–43 mmHg), and pH (7.35–7.45). A catheter was inserted into the femoral vein for anesthesia and paralytic infusion. A tracheotomy was performed, and rats were ventilated with a mixture of air and oxygen. A (3×3)-mm^2 cranial window was opened in the parietal bone, and the dura was removed. To label the cortical astrocytes, we topically applied the red fluorescent dye Sulforhodamine 101 (SR101, Sigma-Aldrich, St. Louis, Missouri, 100-μM concentration) to the exposed cortical surface.[19] The cranial window was subsequently rinsed, filled with 1.5% agarose, and sealed with a 150-μm-thick microscope coverslip. During the measurement, isoflurane was discontinued and anesthesia was maintained by first injecting a 50-mg/kg intravenous bolus of α-chloralose followed by continuous intravenous infusion at 40 mg/(kg h). To reduce possible animal motion during experiments, we administered an intravenous bolus of pancuronium bromide (2 mg/kg) followed by continuous intravenous infusion at 2 mg/(kg h). All experimental procedures were approved by the Massachusetts General Hospital Subcommittee on Research Animal Care.

Hypoxia (17 experimental trials) was created by reducing the fraction of inspired oxygen (FiO$_2$) from 21% (normoxia) to 14.7–16.8% (20–30% reduction of O_2 content from normoxic condition). Hyperoxia (three experimental trials) was created by increasing the fraction of inspired oxygen (FiO$_2$) from 21% (normoxia) to 100%. Finally, respiratory arrest was created by stopping the ventilator for a brief period of time. Simultaneous imaging of NADH and SR101 fluorescence was performed 50–110 μm below the cortical surface using an excitation wavelength of 740 nm. No signs of NADH or SR101 bleaching were detected during imaging. Hypoxia experiments consisted of a 3-min-long normoxic baseline followed by a 7-min-long hypoxia. NADH and SR101 fluorescence intensity was acquired in detection channels having emission filters with 460 ± 25 and 595 ± 25 nm transmission bands, respectively [Fig. 1(b)]. The imaging frames were 512×512 pixels ($466 \times 466 \, \mu$m^2), the pixel dwell time was 4 μs, and the acquisition time of each frame was 1.7 s. Arterial blood gases and pH were measured before and at the end of the hypoxia.

We obtained structural images of the cortical vasculature after experiments by labeling blood plasma with dextran-conjugated fluorescein (FITC; FD2000S, Sigma-Aldrich; St. Louis, Missouri, 500-nM concentration in blood) and performing TPLSM imaging with 1-μm axial steps. The microvascular graphs were subsequently obtained following the procedure from Fang et al.[20]

Fig. 1 (a) Schematic of the cortical surface. Excitation and detection cones are defined by objective NA. (b) Normalized emission spectra of NADH and SR101 (thick solid lines), transmission of emission filters in NADH and SR101 detection channels (dashed lines), and HbO and HbR molar extinction coefficients (thin solid lines).

2.3 Modeling Two-Photon Laser Scanning Microscopy Fluorescence Excitation and Emission in Cortical Tissue

2.3.1 Detection of fluorescence intensity emission

We assume that two-photon excitation of fluorescence is confined to the vicinity of the excitation beam focus and consider imaging depths up to 150 μm below the cortical surface. For these shallow imaging depths and for a 400–650 nm fluorescence emission spectral range [Fig. 1(b)], ray-tracing algorithms provide a satisfactory alternative for modeling the propagation and detection of fluorescence emission.

In our ray-tracing procedure, rays of emitted fluorescence from the excitation beam focus were assigned to the axes of cones with the small solid angle [$\Delta\Omega$, Fig. 1(a)], uniformly distributed in the detection cone defined by the objective NA. The uniform ray separation was achieved by setting a distance of 1 μm between rays at the surface of the spherical insert of the detection cone. The space occupied by the cortical tissue was discretized using 1-μm^3 voxels; optical absorption and scattering coefficients were set in accordance with the realistic 3-D microvascular structure. We assumed uniform optical properties of the gray cortical matter outside the blood vessels. Blood optical absorption was estimated assuming that oxy-hemoglobin (HbO) and deoxy–hemoglobin (HbR) were the only absorbers in the blood. Hematocrit (HcT) values of the individual microvessels were calculated based on the vessel diameter and measurement data from Lipowsky et al.[21,22] and are summarized in Table 1. We were primarily interested in estimating relative changes of the detected NADH signal due to hemodynamic changes and with

Table 1 Hematocrit and optical scattering coefficient of the whole blood as a function of the microvascular diameter.

Diameter (μm)	Hematocrit (%)	μ_s (mm^{-1})
7	7.7	79
10	8.5	86
15	9.7	97
20	10.8	107
30	13.5	129
50	20.3	180
80	34.2	250

respect to microvascular structures [Fig. 1(a)]. Consequently, only absorption of the emitted fluorescence inside the microvasculature was taken into account by the ray-tracing detection algorithm. The effects of optical scattering and absorption in the extravascular space were common for all locations at the same imaging depth. The importance of optical scattering was further minimized by the shallow imaging depths and by applying detection optics with a large etendue in TPLSM.

The detected fluorescence intensity of dye i in the detector channel D_i from a single optical ray in direction $\hat{\Omega}$ is given by

$$\Delta I_{D_i} = I_{0,i} \frac{\Delta\Omega}{4\pi} \Gamma_{D_i} \int_\lambda d\lambda T_{D_i}(\lambda) E_{D_i}(\lambda) \exp\left[-\int_0^{l_{\hat{\Omega}}} \mu_a(l,\lambda)dl\right],$$
(1)

where we neglected cross-talk signals from additional fluorophores simultaneously present in the tissue and a constant background signal due to stray light, detector dark current, and amplifier offset. In Eq. (1) $I_{0,i}$ is the total fluorescence intensity emitted from the focal volume, $\Delta\Omega/4\pi$ represents the fraction of isotropically emitted fluorescence in a solid angle $\Delta\Omega$ directed toward the detector [Fig. 1(a)], Γ_{D_i} is the detector sensitivity including detector quantum efficiency and gain (assumed to be constant across the bandwidth of the emission filter), T_{D_i} is the combined transmission of the optical elements in the detection pathway, E_{D_i} is the emission spectrum of the dye [Fig. 1(b)], and $\mu_a(l,\lambda)$ is the optical absorption coefficient along the ray of length $l_{\hat{\Omega}}$ at distance l from the focus. $\mu_a(l,\lambda)$ can be further expressed as $C_{\text{HbT}}(l)\varepsilon_{\text{SO}_2}(l,\lambda)$ where $C_{\text{HbT}}(l)$ is whole blood molar concentration of total hemoglobin (HbT) and $\varepsilon_{\text{SO}_2}(l,\lambda)$ is the molar extinction coefficient of hemoglobin at oxygen saturation SO$_2$ and wavelength λ. Total detected fluorescence intensity was obtained by adding the contribution from all rays within the detection cone as

$$I_{D_i} = \frac{I_{0,i}}{4\pi} \Gamma_{D_i} \sum_{\hat{\Omega}_j \in \Omega_{\text{NA}}} \Delta\Omega \int_\lambda d\lambda T_{D_i}(\lambda) E_{D_i}(\lambda)$$

$$\times \exp\left[-\int_0^{l_{\hat{\Omega}_j}} \mu_a(l,\lambda)dl\right],$$
(2)

where Ω_{NA} is the solid angle associated with the objective NA. In Eq. (2) we performed a summation of all of the rays $\hat{\Omega}_j$ inside the detection cone. We assumed that the detection optical system accepts all optical rays collected by the objective. All ray-tracing calculations were implemented in MATLAB (The MathWorks, Inc., Natick, Massachusetts).

2.3.2 *Fluorescence excitation*

Because of the nonlinear nature of two-photon fluorescence excitation, optical scattering is one of the key parameters determining TPLSM imaging performance.[23–26] Even highly forward-scattering events, such as scattering from red blood cells (RBCs), can sufficiently divert photon trajectories and significantly reduce nonlinear excitation at the focus. Although the effect of optical scattering on the TPLSM signal has been recognized and studied extensively in the case of a spatially uniform distribution of optical parameters,[23,25–27] the effect of scattering from heterogeneously distributed RBCs has not been quantified. Large shadows in detected fluorescence can be seen underneath the blood vessels in virtually all *in vivo* TPLSM brain images,[7,18] and the highest imaging penetration depths can be obtained only by positioning the field of view away from the large pial vessels. Both hemoglobin absorption of the fluorescence emission and reduction of excitation due to RBC scattering contribute to decay of the detected signal underneath the blood vessels. In contrast to modeling detection of the visible fluorescence emission, attenuation of near-infrared excitation light due to hemoglobin absorption can be neglected. Finally, absorption and scattering of excitation light in the tissue around the vessels can be neglected because its contribution is common to all voxels at the same imaging depth.

We used a modification of the classic ray-tracing algorithm[28] to estimate average excitation intensity at the focus. We first created uniformly distributed excitation rays with a spatial distribution determined by the objective NA by following the same procedure as for emission detection. The rays were traced from the sample surface toward the excitation focus. The initial weight of each ray was calculated assuming the Gaussian profile of the excitation beam intensity – $I(r) = I_0 \exp(-2r^2/\omega^2)$ – where ω is the beam waist at the back aperture of the objective. To account for the scattering from the RBCs, we introduced the following modification to the ray-tracing procedure: the probability p_s of a scattering event was calculated inside each vessel along the ray as $p_s = 1 - \exp(-\mu_s l)$, where μ_s is the optical scattering coefficient of blood for a given hematocrit and l is the ray path length inside the vessel. We further defined an excitation disk in the focal plane around the focus. The excitation disk radius $R_E = 1.08\omega_0$ was set at ∼10% of the focal peak intensity, where ω_0 is the beam waist at the focus. The probability p_e that the ray scattered inside the blood vessel will cross the excitation disk was calculated assuming the Henyey–Greenstein scattering phase function as

$$p_e = \frac{1+g}{2g}\left[1 - \frac{1-g}{\sqrt{1+g^2-2g\cos(\alpha)}}\right], \qquad (3)$$

where g is scattering anisotropy and α is an average half-angle of a cone defined by the scattering event location and the excitation disk perimeter. The initial weight of each ray was then multiplied by a probability $p = 1 - p_s + p_s p_e$ that the ray will

intersect with the excitation disk. This procedure captures the first-order scattering of the excitation light, which is a dominant effect in *in vivo* cortical NADH imaging. The scattering length in microvessels (∼6–12 μm; Table 1) is comparable to the capillary diameter[24,29,30] (∼8 μm), and the probability of the ray passing through more than one blood vessel at small imaging depths is small. The total fluorescence intensity $I_{0,i}$ [Eq. (2)] emitted from the focal volume ΔV was calculated in the ray-tracing algorithm as

$$I_{0,i} = \frac{1}{2}\Phi_i C_i \left[\sum_{\hat{\Omega}_j \in \Omega_{NA}} p(\hat{\Omega}_j) I_e(\hat{\Omega}_j) d\Omega\right]^2 \delta \Delta V, \qquad (4)$$

where $\Phi_i/2$ is the dye quantum yield in two-photon excitation, C_i is the dye concentration, δ is the two-photon absorption cross section, $I_e(\hat{\Omega}_j)$ is the initial intensity of the ray assuming a Gaussian excitation beam profile, and $p(\hat{\Omega}_j)$ is the probability that the ray intersects with the excitation disk.

2.3.3 *Modeling of two-photon laser scanning microscopy excitation of fluorescence in cortical tissue by Monte Carlo simulation*

We modified the fast Monte Carlo code based on a graphics processing unit (GPU) for photon migration in optically turbid media[31] to include excitation by a focused beam with a Gaussian intensity profile. The realistic 3-D microvascular structures were imported into the Monte Carlo (MC) simulation, and values of optical absorption and scattering were assigned to the intra- and extravascular space. The voxel size in the simulation was 1 μm^3. Photon positions at time intervals corresponding to a 0.5-μm step were recorded, and a four-dimensional spatiotemporal distribution of photons $G(\mathbf{r}, \mathbf{t})$ arising from an infinitely short excitation pulse was recorded. We assumed a 200-fs-wide excitation pulse and performed a convolution of $G(\mathbf{r}, \mathbf{t})$ with the temporal profile of the excitation pulse to obtain the spatiotemporal distribution of the photons $I_{exc}(\mathbf{r}, \mathbf{t})$ in the medium.[27] Finally, fluorescence excitation was estimated by integrating $I_{exc}^2(\mathbf{r}, \mathbf{t})$ over time and adding the contribution of all spatial voxels within $\pm 10 \mu$m of the focus. The spatial distribution of the fluorophores was considered uniform. The initial photon directions toward the focus were randomly perturbed to form a Gaussian intensity profile in the focal plane in scattering free media. The beam waist at the focus was determined by the objective NA, 740-nm excitation wavelength, and the excitation beam truncation ratio (i.e., the ratio of the excitation beam waist before the objective to the objective back aperture radius). This procedure is successful in overcoming the absence of optical diffraction in a traditional MC simulation and its subsequent effects on the intensity distribution in the focal plane. Matching the axial intensity profile around the focus in a MC simulation is, however, considerably more challenging and our MC code did not account for it.
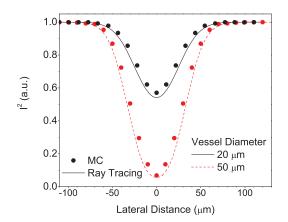
3 Results and Discussion

3.1 *Justification of the Ray-Tracing Procedure*

We compared our modeling of the fluorescence emission detection using ray-tracing to MC simulations. The fluorescence emission was generated isotropically from the focal volume, and the parameters for the detection optics were based on the

Olympus XLUMPLFL 20X objective (NA = 0.95). We assumed realistic average brain tissue optical properties[14–17] (μ_s = 19.4 mm^{-1}, $g = 0.9$, $\mu_a = 1.6$ mm^{-1} at 450 nm; $\mu_s = 13.8$ mm^{-1}, $g = 0.9$, $\mu_a = 0.12$ mm^{-1} at 600 nm). For a 10–200 μm range of imaging depths, the error of the number of detected ray-traced photons is between -30 and $+20\%$. However, in this work we are primarily interested in estimating relative changes in detected NADH fluorescence from the shallow imaging depths. In addition, the effect of hemodynamic responses on fluorescence emission is exerted predominantly through the changes in optical absorption of blood. Therefore, neglecting scattering in the detection ray-tracing algorithm has little effect on the relative changes in NADH fluorescence signal in our simulations.

We found excellent agreement between our ray-tracing excitation procedure and the MC simulation results of the excitation beam. In Fig. 2, relative changes of the squared excitation intensity at the focus are presented as a function of lateral distance from the pial vessel axis in an imaging plane at a depth of 100 μm. The pial vessels were positioned parallel to the tissue surface with a depth of vessel axis equal to the vessel radius [Fig. 1(a)]. Both the ray-tracing algorithm and the MC simulation used the parameters of the Olympus XLUMPLFL 20X objective (NA = 0.95, focal length = 9 mm, back aperture diameter = 17.1 mm) and a Gaussian intensity profile of the excitation beam with a 4.5-mm beam waist measured in our experimental setup. The overlap of the excitation profiles of the two simulation methods confirms the appropriateness of using only the first-order scattering and the excitation radius in our ray-tracing algorithm.

Scattering from RBCs in blood is highly anisotropic, and the scattering coefficient is high compared to the brain tissue. In addition, due to tight RBC packing, optical waves in the visible and near-infrared wavelength ranges experience simultaneous (dependent) scattering from multiple RBCs.[10,11,13] However, using a scattering anisotropy in blood of $g = 0.99$,[10–13] a scattering coefficient of $\mu_s = k(1 - \text{HcT})\text{HcT}$,[32] where k is a proportionality constant, and $\mu_s = 275$ mm^{-1} at HcT = 0.45 and an excitation wavelength of 740 nm,[10,12] we have found good agreement between our simulated profiles of detected NADH

and SR101 fluorescence intensities and our experimental measurements. Other combinations of g and μ_s (e.g., $g = 0.98$, $\mu_s = 137$ mm^{-1}) are also appropriate, as long as the value of the reduced scattering coefficient $\mu_s' = \mu_s(1 - g)$ is approximately conserved, and their choice should have little influence on relative changes in the fluorescence signal in our imaging configuration. Figure 3 presents an example comparing our ray-tracing algorithm to experimental data. On the basis of *in vivo* anatomical microvascular images [Fig. 3(a)], we constructed a graph of the microvasculature[20] and obtained locations and diameters of microvessels [Fig. 3(b)]. Two-dimensional profiles of NADH and SR101 fluorescence intensities at a depth of 110 μm below the rat cortical surface simultaneously obtained in the TPLSM experiment are presented in Figs. 3(c) and 3(e), respectively. The corresponding NADH and SR101 fluorescence intensity profiles along the lines marked with white dots in Figs. 3(c) and 3(e) are presented in Figs. 3(d) and 3(f), respectively. On the basis of the microvascular graph [Fig. 3(b)], we estimated HcT and μ_s in all microvessels and performed the full ray-tracing simulation (including excitation and detection of fluorescence intensity). Unlike our comparison between experiments and the full ray-tracing simulations, we found that simulations of the fluorescence emission detection only (i.e., accounting only for blood absorption of the emission signal) failed to explain large intensity shadows measured underneath the blood vessels.

Our ray-tracing algorithm takes into account first-order scattering of excitation light and absorption of fluorescence emission from the blood. These mechanisms are dominant when estimating the relative change of detected fluorescence intensity in TPLSM imaging at the same imaging depth as a function of microvascular structure and hemodynamic changes, while blood absorption of excitation light as well as tissue scattering and absorption can be neglected. We also assumed that changes in the optical scattering coefficient in extravascular space due to possible cell swelling during functional activation (e.g., whisker and forepaw stimulation) have a minor effect on the TPLSM imaging of cortical NADH fluorescence. Although we could implement a full MC simulation in both excitation and detection of fluorescence intensity, ray tracing offered simplicity and, more importantly, much greater speed of calculations. Furthermore, both MC simulations and experimental data were found to agree well with full ray-tracing simulations. We therefore relied on ray-tracing algorithms to obtain the following data.

3.2 Detected NADH Fluorescence and the Influence of Pial Vessel Diameter, Objective NA, Imaging Depth, and Lateral Distance from the Vessel

In all simulations hereafter, we assumed an excitation beam waist equal to the radius of the objective back aperture (overfilled back aperture) and, if not specified, NA = 0.95 and SO$_2$ = 0.75. Figures 4(a)–4(c) show relative NADH fluorescence intensity as a function of pial vessel diameter (5–80 μm), imaging depth (20–100 μm), and lateral distance. Figures 4(d) and 4(e) summarize the information from Figs. 4(a)–4(c) by showing the contour lines at 50 and 90% of the maximum fluorescence intensity obtained versus the lateral distance. The intensity values below large vessels (≥ 50 μm) approach zero even at imaging depths greater than the vessel diameter. The lateral extent of
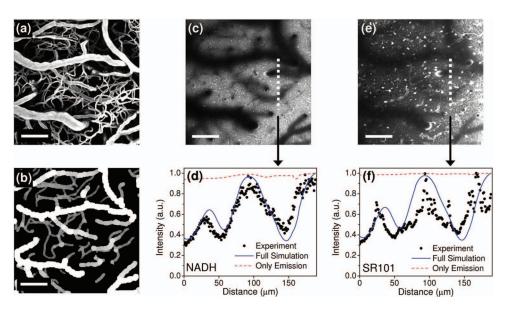

Fig. 2 Two-photon excitation of fluorescence in cortical tissue below the pial blood vessel. Monte Carlo simulations (dots) and ray-tracing algorithms (lines) were used to estimate two-photon excitation line profiles 100 μm below the pial blood vessels with diameters of 20 μm (solid line) and 50 μm (dashed line).

Fig. 3 Comparison of the ray-tracing algorithm with the experimental data. (a) Maximum intensity projection (MIP) of a 400-μm-thick microvascular stack labeled with FITC in rat primary somatosensory cortex. (b) MIP of the 110-μm-thick reconstructed microvasculature obtained from (a) using microvascular graphing. Vessel diameters were presented with different shades of gray. (c, e) TPLSM images of NADH and SR101 fluorescence intensities at a depth of 110 μm. Scale bars are 100 μm. (d, f) Fluorescence intensity profiles (black dots) along the white dotted lines from (c) and (e), respectively. Solid lines represent the results of the full ray-tracing algorithms (fluorescence excitation and emission detection), while dashed lines represent ray-tracing results based on blood absorption of emission detection only.

the intensity shadow increases several tens of microns with the increasing imaging depth. The detected fluorescence within the shadow reaches a minimum value at a depth comparable to the vessel diameter. Relatively small shadows can be observed underneath the smallest microvessels (intensity decreases $< 10\%$ for a vessel diameter of < 6 μm), but small arterioles and venules (diameter ~ 20 μm) can decrease the detected fluorescence by 50%. Finally, increasing the objective NA is often desirable in TPLSM imaging. However, larger NA increases the lateral extent of the intensity shadows, with a greater rate of increase at greater imaging depths, which makes NADH fluorescence imaging more vulnerable to distortions from the vasculature.

3.3 Changes in Blood Volume and Hemoglobin Oxygen Saturation Modulate the Detected NADH Fluorescence
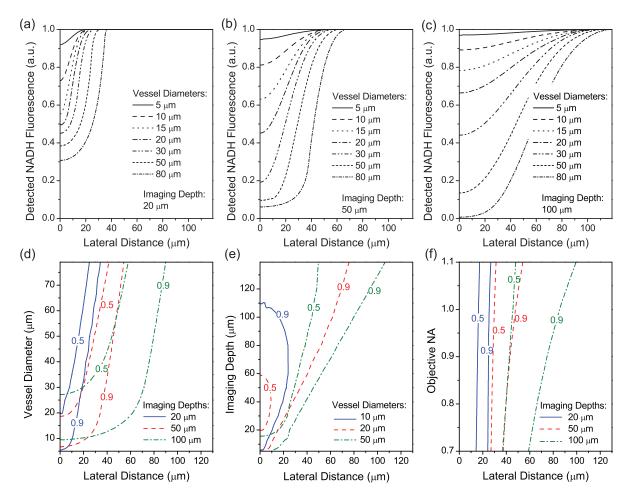
During functional brain activation, changes in NADH concentration are typically accompanied by hemodynamic responses (changes in cerebral blood flow, volume, and oxygen saturation of hemoglobin). Blood flow increases can be as large as $\sim 60\%$ during functional activation of primary somatosensory cortex (e.g., forepaw stimulation), with corresponding blood volume changes of up to $\sim 20\%$ and NADH changes up to $\sim 4\%$.[4,33–35] Figure 5 shows relative changes of detected NADH fluorescence intensity as a function of total blood volume changes and SO$_2$ changes for pial vessels with diameters of 10, 20, and 50 μm and at imaging depths of 20, 50, and 100 μm. In our ray-tracing procedure, we approximated the blood volume changes by changing the total hemoglobin concentration (HbT) (i.e., changing the hematocrit and neglecting changes in vessel diameters). Figures 5(a)–5(c) show relative changes in detected NADH fluorescence intensity (rNADH) assuming $\pm 20\%$ changes in HbT and no change in NADH concentration. In all

cases [Figs. 5(a)–5(c)] changes in HbT were capable of producing NADH signal changes comparable to or greater than expected brain-activation–induced NADH concentration changes. The largest effect was observed directly underneath the vessels and in the presence of the larger vessels. Contrary to the changes in HbT, even relatively large SO$_2$ changes [Figs. 5(d)–5(f)] had an approximately one order-of-magnitude smaller effect on the detected NADH signal. This is largely due to the marginal influence of SO$_2$ changes on the optical scattering of blood, but also due to relatively similar contributions of HbO and HbR to absorption of NADH fluorescence emission within the bandwidth of our emission filter [Fig. 1(b)]. In the following analysis, we therefore restrict the consideration of hemodynamic responses to the influence of HbT changes. However, we note that SO$_2$ changes cannot be neglected immediately underneath the larger vessels [diameter > 20 μm; Figs. 5(d) and 5(e)].

Figure 6 shows the relative errors of detected NADH signal assuming a true $+2\%$ NADH fluorescence change and a simultaneous $\pm 20\%$ HbT change. For all combinations of vessel diameters and imaging depths (except for the pial vessel with a 10-μm diameter and imaging depth of 100 μm), we have observed that the confounding influence of rHbT can change the sign of the measured NADH fluorescence signal (i.e., an error worse than -100%) or produce an error larger than $+100\%$. Figures 6(a)–6(i) provide a range of lateral distances for a given vessel diameter and imaging depth where NADH imaging is either very strongly or minimally affected by changes in the hemoglobin concentration.

3.4 NADH Fluorescence Intensity Correction Procedure

Two-photon microscopes are typically equipped with at least two detection channels, and most TPLSM experiments, including

Fig. 4 Dependence of detected relative NADH fluorescence intensity on microvascular structure and imaging parameters. (a–c) Relative NADH fluorescence intensity dependence on vessel diameter (5–80 μm) and lateral distance at imaging depths of 20, 50, and 100 μm, respectively. (d, e) summarize the information presented in (a–c). Contour lines represent 50 and 90% intensity levels. (f) Influence of objective NA on detected relative NADH signal in the presence of the pial vessel with 50-μm diameter at three imaging depths (20, 50, and 100 μm).

TPLSM imaging of NADH fluorescence, involve simultaneous imaging of more than one fluorophore. Typically, at least one fluorophore is used for labeling of the morphological features of the tissue and this generally does not change in response to tissue physiology (i.e., the fluorophore is physiologically inert). This allows us to explore the idea of utilizing the changes in the fluorescence signal of a physiologically inert fluorophore[36] to correct the NADH measurements corrupted by HbT changes. In our measurements, Sulforhodamine 101 (SR101) was used to label cortical astrocytes (Figs. 3 and 9). SR101 was excited and its fluorescence was recorded simultaneously with the NADH signal. The emission spectra of SR101 and NADH are well separated, minimizing the cross-talk between their detection channels. The concentration and physical properties of SR101 were assumed to be independent of the physiological changes in cortical tissue. Finally, we were able to reproduce the results of Figs. 4–6 for the SR101 detection channel, confirming the dominant role of HbT changes on detection of relative SR101 fluorescence intensity.

The detected fluorescence intensity I_{D_i} of fluorophore i in detection channel D_i can be expressed [Eqs. (2) and (4)] as $I_{D_i} = C_i F_i$, where C_i is the con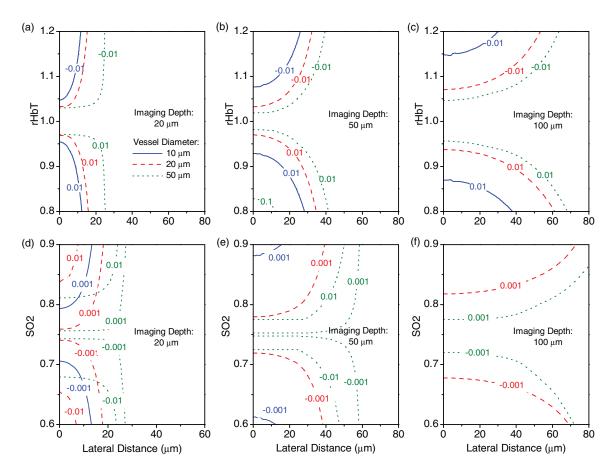centration of fluorophore i, and F_i accounts for the properties of the optical excitation and detection system, fluorophore two-photon absorption cross section, quantum yield, etc. The detected relative changes in NADH and SR101 fluorescence during brain activation can be further expressed as

$$\frac{\Delta I_{\text{NADH}}}{I_{\text{NADH}}} = \frac{\Delta C_{\text{NADH}}}{C_{\text{NADH}}} + \frac{1}{F_{\text{NADH}}} \frac{\partial F_{\text{NADH}}}{\partial C_{\text{HbT}}} \Delta C_{\text{HbT}}, \qquad (5)$$

$$\frac{\Delta I_{\text{SR101}}}{I_{\text{SR101}}} = \frac{1}{F_{\text{SR101}}} \frac{\partial F_{\text{SR101}}}{\partial C_{\text{HbT}}} \Delta C_{\text{HbT}}, \qquad (6)$$

where ΔI_{NADH} and ΔI_{SR101} are changes in detected NADH and SR101 fluorescence intensities, respectively, ΔC_{HbT} is the change in intravascular HbT concentration (blood volume) induced by the hemodynamic response, and ΔC_{NADH} is the change in the NADH concentration. By substituting ΔC_{HbT} from Eq. (6) into Eq. (5), we obtain the expression for the relative NADH concentration change as

$$\frac{\Delta C_{\text{NADH}}}{C_{\text{NADH}}} = \frac{\Delta I_{\text{NADH}}}{I_{\text{NADH}}} - K \frac{\Delta I_{\text{SR101}}}{I_{\text{SR101}}}, \qquad (7)$$
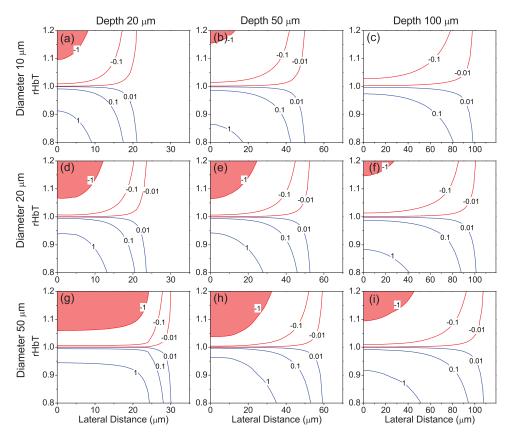
Fig. 5 Influence of blood volume and hemoglobin oxygen saturation changes on the detected NADH fluorescence intensity given no changes in NADH concentration. (a–c) Influence of ±20% changes in HbT on the NADH signal. (d–f) Influence of SO_2 changes on the NADH signal. The relative changes in the NADH signal in (d–f) were calculated with respect to $SO_2 = 75\%$. Contour lines represent ±0.1, ±1, and ±10% changes in detected NADH fluorescence intensity as a function of lateral distance, relative HbT (rHbT), SO_2, pial vessel diameter (10, 20, and 50 μm) and imaging depth (20, 50, and 100 μm).

where the correction factor K is given by

$$K = \frac{\partial F_{NADH}/\partial C_{HbT}}{F_{NADH}} \frac{F_{SR101}}{\partial F_{SR101}/\partial C_{HbT}}. \quad (8)$$

Figure 7 shows the correction factor K as a function of vessel diameter, imaging depth, and lateral distance from the vessels. The presented values of the coefficient K were obtained from Eq. (7) by using the ray-tracing procedure and estimating the values of $\Delta I_{NADH}/I_{NADH}$ and $\Delta I_{SR101}/I_{SR101}$ for $\Delta C_{HbT}/C_{HbT} = +20\%$, and $\Delta C_{NADH} = 0$. Higher values of K were observed for greater vessel diameters and shorter lateral distances. Also, K values closer to 1 were observed at greater imaging depths and farther from the vessels. On the right-hand side of in Figs. 7(a)–7(c), K was set to 1 at lateral distances where excitation and emission cones did not intersect the vessels since at these locations $\Delta I_{SR101} = 0$ and K in Eq. (7) is not defined. However, because $\Delta I_{SR101} = 0$, any value of K at these locations will provide a correct estimate of the NADH fluorescence change. Importantly, the dependence of K on C_{HbT} is very weak. Calculating the data presented in Fig. 7 for $\Delta C_{HbT}/C_{HbT} \in (-0.2, 0.2)$ revealed only a few percent change in the values of the correction factor.

We also explored a much simpler approach to correction of the NADH measurements based on a single value for the correction factor K. Figure 8 shows the relative errors of the corrected NADH fluorescence intensity changes given a +2% true NADH fluorescence change and simultaneous ±20% changes of C_{HbT}, and using a correction factor of $K = 1.15$. This value was found empirically by searching the space of parameters presented in Fig. 8 to minimize the overall error of the corrected NADH signal. The main criterion for choosing the value of correction factor K was to achieve a relative measurement error better than -100% underneath smaller vessels, which are virtually impossible to avoid inside the excitation and emission cones in TPLSM. Values of K that are <1.10 provide insufficient correction, and errors in NADH measurements in excess of ±100% are present underneath both large and small vessels, approaching the situation presented in Fig. 6. Values of K that are >1.45 provide improvement in measurement error beneath larger vessels (>50 μm) by reducing the space around the vessels with error greater than ±100%. However, $K > 1.45$ provides large overcompensation of the signal underneath the smaller vessels (diameter < 50 μm) and creates errors that exceed ±100%. For $1.10 < K < 1.40$, no errors worse than ±100% are present for all vessels with diameters of ≤ 20 μm and at all depths. For

Fig. 6 Influence of blood volume changes on the detected NADH fluorescence intensity assuming a true +2% change in NADH fluorescence. (a–i) show the relative error of the detected change in NADH fluorescence intensity (ΔNADH/NADH$_0$) given a $\pm 20\%$ range of change in HbT, different vessel diameters (10, 20, and 50 μm), and imaging depths (20, 50, and 100 μm) as a function of lateral distance. Contours show the relative NADH error of ± 1, ± 10, and $\pm 100\%$. Shaded regions signify the importance of a $\leq -100\%$ detection error, where measurements affected by the HbT changes show the opposite sign from the true NADH fluorescence changes.

this set of K values, the minimum relative error underneath the small vessels was found for $K = 1.15$, with the correction becoming progressively worse with an increase in K. Note that by following this simple correction procedure shaded regions in Fig. 8 with relative error $< -100\%$ were greatly diminished in comparison to the uncorrected data presented in Fig. 6. Only the measurements through or immediately underneath the largest vessels were still associated with very large errors [diameter ≥ 50 μm; Figs. 8(g) and 8(h)]. Importantly, measurement errors below the smallest vessels (diameter ≤ 10 μm) were $< 10\%$ at all imaging locations, indicating that data correction is very good when measurement location is inside the capillary bed.

In addition, measurement errors even in the close proximity of vessels with diameters of 20 μm (smaller arterioles and venules) never exceeded $\pm 100\%$, indicating that at least the sign of the measured NADH signal change will be accurate.

The estimated value of the correction factor is applicable to different animal species (e.g., rats and mice), and based on results presented in Fig. 4(f), it should be minimally dependent on the numerical aperture of the imaging objective at shallow imaging depths. However, use of different emission filters and, especially, application of different physiologically inert fluorophores may warrant new estimation of the correction factor.
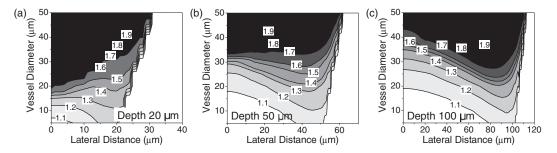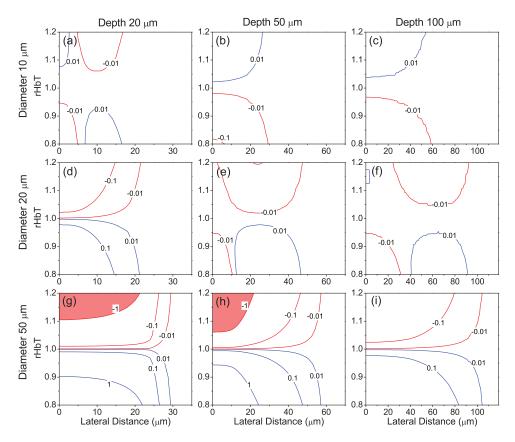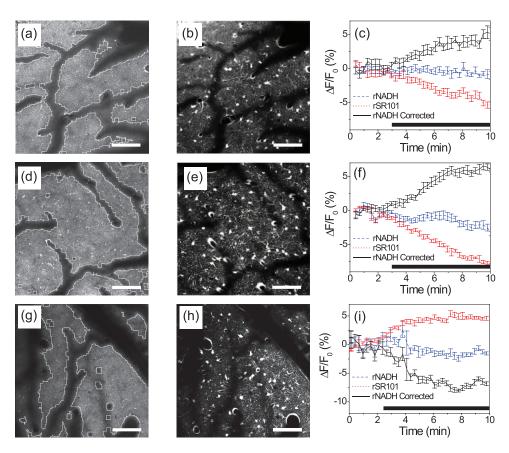

Fig. 7 Correction factor distribution as a function of lateral distance, pial vessel diameter, and imaging depth. The contour lines and gray intensity levels mark the values of the correction factor from 1 to 1.9.

Fig. 8 Influence of blood volume changes on the detected NADH fluorescence intensity using our correction procedure given a +2% true change in NADH fluorescence. (a–i) show the relative error of the corrected change in NADH fluorescence intensity (ΔNADH/NADH$_0$) given a ±20% range of change in HbT, different vessel diameters (10, 20, and 50 μm) and imaging depths (20, 50, and 100 μm) as a function of lateral distance. Contours show the relative NADH error of ±1, ±10, and ±100%. Shaded regions signify the importance of a $\leq -100\%$ detection error, where measurements affected by the HbT changes show the opposite sign from the true NADH fluorescence changes. The value of the correction factor was 1.15.

3.5 *Correction to Two-Photon Laser Scanning Microscopy Imaging of NADH Fluorescence Changes During Mild Hypoxia and Hyperoxia in Rats*
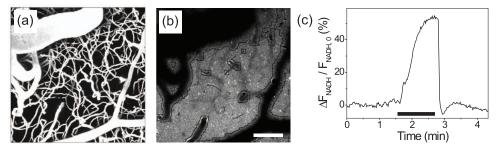
Figure 9 shows three examples of the simple correction procedure applied to the measurement of NADH fluorescence changes during mild hypoxia and hyperoxia in rats. The baseline fluorescence intensities of NADH and SR101 during normoxia are presented in Figs. 9(a), 9(d), and 9(g), respectively. After the initial ∼3 min. of normoxia, mild hypoxia was induced by reducing the normal oxygen content from FiO$_2$ = 21% (normoxia) to FiO$_2$ = 16.8% [Figs. 9(a)–9(c)] and FiO$_2$ = 14.7% [Fig. 9(d)–9(f)]. Similarly, hyperoxia was induced by increasing the normal oxygen content from normoxia to FiO$_2$ = 100% [Figs. 9(g)–9(i)]. A motion-correction procedure written in MATLAB was applied to the raw intensity images to correct the animal motion. Data sets with pronounced axial motion, which could not be corrected by our motion-correction procedure, were discarded. The spatial heterogeneity of the SR101 staining is very helpful in guiding the motion correction procedure. The relative NADH and SR101 fluorescence intensity changes during experiments were spatially averaged within the selected regions of interest [(ROIs) marked with white lines in Figs. 9(a), 9(d), and 9(g) that exclude only the large shadows from the vasculature]; their temporal traces are presented in

Figs. 9(c), 9(f) and 9(i), respectively. In response to the reduced FiO$_2$, blood flow and blood volume in cortical microvasculature increased, creating a clear reduction in the detected SR101 signal. Although severe hypoxia or complete respiratory arrest (Fig. 10) can induce more than a 20% increase in NADH fluorescence intensity, our experiments with mild hypoxia (20–30% reduction in inspired O$_2$ content from normoxia) produced only a few percent increase in the NADH signal, comparable to the signal change that is expected in experiments with functional brain activation. Although estimation of the true NADH concentration change based on the fluorescence intensity change is not trivial due to the existence of several NADH fluorescence lifetimes in different cellular compartments and molecular environments, hypoxic conditions generally lead to an increase in both NADH concentration and fluorescence emission, with the increase in NADH fluorescence two- to threefolds smaller than the actual increase in NADH concentration.[8] However, as expected, on the basis of our ray-tracing simulations, hemodynamic changes significantly affected the mild changes in NADH fluorescence intensity, as shown in Figs. 9(c) and 9(f), and the noncorrected temporal traces of the NADH signal changes showed no clear indication of the expected NADH increase. After we applied the simple correction procedure (i.e., $K = 1.15$), NADH fluorescence intensity increases during hypoxia were restored in all ROIs. The in-

Fig. 9 Correction procedure applied to the detected NADH fluorescence intensity changes during mild hypoxia and hyperoxia. (a–c) Mild hypoxia with $FiO_2 = 16.8\%$. (a, b) NADH and SR101 fluorescence intensities, respectively, 55 μm below cortical surface. (c) Temporal profiles of relative noncorrected NADH and SR101 fluorescence intensity changes from the ROIs outlined by white lines in (a) and the corresponding corrected NADH signal obtained by using simple correction procedure with $K = 1.15$. An initial $\sim$3 min. of normoxia ($FiO_2 = 21\%$) was followed by 7 min. of mild hypoxia ($FiO_2 = 16.8\%$). The hypoxic period is marked by the black bar in (c). (d–f) Mild hypoxia with $FiO_2 = 14.7\%$, 50 μm below cortical surface. (g–i) Hyperoxia with $FiO_2 = 100\%$, 70 μm below cortical surface. Scale bar: 100 μm.

crease of the NADH fluorescence signal reaches steady state a few minutes after the start of the mild hypoxia. We estimated an $\sim$3.5% increase in the corrected NADH signal with $FiO_2 = 16.8\%$ [Fig. 9(c)] and an $\sim$5.5% increase with $FiO_2 = 14.7\%$ [Fig. 9(f)]. In response to the increased FiO_2 in hyperoxia experiments [Figs. 9(g)–9(i)] vasoconstriction of arterial branches induced decreased flow and blood volume in cortical microvas-

culature, creating a clear increase in the detected SR101 signal. Increased oxidation of NADH resulted in decreased detected NADH fluorescence, which was masked by the blood volume changes (Fig. 9(i), dashed line). The application of the correction procedure revealed a decrease in NADH fluorescence that reached steady state at $\sim -7.5\%$ a few minutes after the start of hyperoxia.

Fig. 10 NADH fluorescence emission intensity change during respiratory arrest. (a) Maximum intensity projection of a 200-μm-thick microvascular stack labeled with FITC in rat SI cortex. (b) NADH fluorescence intensity map 100 μm below cortical surface. Scale bar: 100 μm. (c) Temporal profile of relative NADH fluorescence intensity changes from the ROI outlined by black line in (b). An initial 95 s of normal breathing ($FiO_2 = 21\%$) was followed by 70 s of respiratory arrest and subsequent return to normal breathing. The respiratory arrest period is marked by the black bar in (c).

4 Conclusion

We present a detailed analysis of the influence of hemodynamic changes on the detection of relative cortical NADH fluorescence changes in TPLSM imaging. The analysis was performed by taking into account the detailed microscopic microvascular anatomy and optical properties of tissue and blood. The choice of our ray-tracing algorithm was justified by its simplicity and computational efficiency, and validated by Monte Carlo simulations. We further validated the ray-tracing method by comparing its predictions to the results of *in vivo* imaging in rat cortex. We compared contributions of the optical scattering from RBCs in the fluorescence excitation pathway and the absorption of fluorescence emission by blood for the creation of the large intensity shadows underneath the pial blood vessels in TPLSM imaging. Our analysis shows that, because of the nonlinear nature of fluorescence excitation in TPLSM, intensity shadows underneath blood vessels are predominantly caused by the widening of the excitation focal spot due to high scattering from RBCs. This scattering effect enhanced by nonlinear excitation does not exist in imaging systems based on linear excitation of fluorescence, but it must be considered when estimating the influence of hemodynamic response on fluorescence emission in TPLSM. The influences of vessel size, imaging objective NA, imaging depth, lateral distance from the vessel, and changes in the blood volume and oxygen saturation in the detected NADH fluorescence intensity were discussed in detail. We have shown that physiological blood volume changes have a significantly stronger effect on the detected fluorescence signal than physiological changes in SO_2. In cases when measurements were taken in close proximity to large vessels, changes in blood volume induced by functional brain activation can result in large measurement errors, in excess of $\pm 100\%$. The maps of the effect of the microvascular environment on the NADH fluorescence signal may be used to guide the design and interpretation of *in vivo* TPLSM measurements of cortical NADH.

We suggest an approach to correcting the NADH measurements based on the fluorescence signal from an additional physiologically inert fluorophore and a correction factor based on the exact microvascular structure. We have further demonstrated that using even a single correction factor independent of microvascular structure significantly reduced errors for the majority of measurement locations.

The effect of the hemodynamic response on the measured NADH fluorescence intensity was recognized in past studies.[1,2] Frequent approaches to correct for the hemodynamic response in imaging systems with linear fluorescence excitation are to correct the measured NADH fluorescence intensity changes with the changes in diffuse reflectance at 366 nm,[37–41] or to scale NADH signal change based on the fluorescence signal from an additional fluorophore.[36,42–44] These correction procedures were not directly applicable to the *in vivo* TPLSM imaging of cortical NADH with high spatial resolution and inside the highly heterogenous microvascular environment. The strategy of using diffuse reflectance will not work in TPLSM imaging because the diffusely reflected light will acquire information from tissue regions up to few hundreds of micrometers distant from the imaging site[45] and will be largely insensitive to the changes in microvascular configuration around the measurement location. Confocal filtering of reflected light may work only up to a few tens of microns in cortical tissue, which will diminish

advantages of *in vivo* TPLSM imaging. Collection of reflected light may generally require significant changes in TPLSM detection systems that can potentially compromise TPLSM imaging. In addition, the nonlinear nature of fluorescence excitation in TPLSM requires a significantly different treatment of the excitation and emission wavelengths.

Utilization of fluorescence emission from an additional, physiologically inert fluorophore for the correction procedure in imaging systems with the linear fluorescence excitation was explored in the past by several groups.[36,43,44,46,47] Methods such as normalized fluorescence ratio[44,46] or double fluorescence ratio[44,47] require either additional measurements when one fluorophore is absent from the tissue or simultaneous excitation at two wavelengths, which are not applicable to *in vivo* TPLSM imaging of cortical NADH. Kramer and Pearlstein[36] used a simpler approach where a physiologically inert fluorophore Rhodamine B was simultaneously excited with NADH fluorescence at 366 nm. The corrected NADH signal was estimated as a ratio of emissions of two fluorophores at the hemoglobin isosbestic points at 448 and 549 nm. Our correction strategy utilized the similar advantage of simultaneous excitation of two fluorophores. This approach is simple to implement with existing multichannel TPLSM detection systems, and simultaneous dual excitation provides an efficient solution for the problem of high sensitivity of the two-photon fluorescence excitation on scattering from the RBCs. Our correction strategy is based on the cortical microvascular environment and, if necessary, can be extended to include the exact correction at each point in space. In contrary, the fluorescence ratio technique developed by Kramer and Pearlstein[36] is insensitive to the microvascular configuration and it fails to adapt to different tissue optical properties.[46] However, it is worth noting that for very small changes in SR101 emission and for values of correction coefficient K close to unity, ratio of SR101 emission signal to NADH emission provides somewhat similar results to our correction technique.

Our simple correction procedure was successfully applied to *in vivo* imaging of NADH fluorescence changes during mild hypoxia and hyperoxia in rats. The correction of the NADH fluorescence signal can be further generalized to TPLSM imaging of other fluorophores, such as imaging of calcium-sensitive dyes.

1. A. Mayevsky and G. G. Rogatsky, "Mitochondrial function *in vivo* evaluated by NADH fluorescence: from animal models to human studies," *Am. J. Physiol.* **292**, C615–C640 (2007).
2. B. Chance, P. Cohen, F. Jobsis, and B. Schoener, "Intracellular oxidation-reduction states *in vivo*," *Science* **137**, 499–508 (1962).
3. L. N. Duysens and J. Amesz, "Fluorescence spectrophotometry of reduced phosphopyridine nucleotide in intact cells in the near-ultraviolet and visible region," *Biochim. Biophys. Acta* **24**, 19–26 (1957).
4. K. A. Kasischke, H. D. Vishwasrao, P. J. Fisher, W. R. Zipfel, and W. W. Webb, "Neural activity triggers neuronal oxidative metabolism followed by astrocytic glycolysis," *Science* **305**, 99–103 (2004).

5. T. H. Chia, A. Williamson, D. D. Spencer, and M. J. Levene, "Multiphoton fluorescence lifetime imaging of intrinsic fluorescence in human and rat brain tissue reveals spatially distinct NADH binding," *Opt. Express* **16**, 4237–4249 (2008).

6. K. A. Kasischke, E. M. Lambert, B. Panepento, A. Sun, H. A. Gelbard, R. W. Burgess, T. H. Foster, and M. Nedergaard, "Two-photon NADH imaging exposes boundaries of oxygen diffusion in cortical vascular supply regions," *J. Cereb. Blood Flow Metab.* **31**, 68–81 (2010).

7. T. Takano, G. F. Tian, W. Peng, N. Lou, D. Lovatt, A. J. Hansen, K. A. Kasischke, and M. Nedergaard, "Cortical spreading depression causes and coincides with tissue hypoxia," *Nat. Neurosci.* **10**, 754–762 (2007).

8. H. D. Vishwasrao, A. A. Heikal, K. A. Kasischke, and W. W. Webb, "Conformational dependence of intracellular NADH on metabolic state revealed by associated fluorescence anisotropy," *J. Biol. Chem.* **280**, 25119–25126 (2005).

9. Q. Yu and A. A. Heikal, "Two-photon autofluorescence dynamics imaging reveals sensitivity of intracellular NADH concentration and conformation to cell physiology at the single-cell level," *J. Photochem. Photobiol. B* **95**, 46–57 (2009).

10. D. J. Faber, M. C. Aalders, E. G. Mik, B. A. Hooper, M. J. van Gemert, and T. G. van Leeuwen, "Oxygen saturation-dependent absorption and scattering of blood," *Phys. Rev. Lett.* **93**, 028102 (2004).

11. D. J. Faber and T. G. van Leeuwen, "Are quantitative attenuation measurements of blood by optical coherence tomography feasible?" *Opt. Lett.* **34**, 1435–1437 (2009).

12. M. Friebel, A. Roggan, G. Muller, and M. Meinke, "Determination of optical properties of human blood in the spectral range 250 to 1100 nm using Monte Carlo simulations with hematocrit-dependent effective scattering phase functions," *J. Biomed. Opt.* **11**, 34021 (2006).

13. A. Roggan, M. Friebel, K. Dorschel, A. Hahn, and G. Muller, "Optical properties of circulating human blood in the wavelength range 400–2500 nm," *J. Biomed. Opt.* **4**, 36–46 (1999).

14. F. Bevilacqua, D. Piguet, P. Marquet, J. D. Gross, B. J. Tromberg, and C. Depeursinge, "*In vivo* local determination of tissue optical properties: applications to human brain," *Appl. Opt.* **38**, 4939–4950 (1999).

15. A. K. Dunn, A. Devor, A. M. Dale, and D. A. Boas, "Spatial extent of oxygen metabolism and hemodynamic changes during functional activation of the rat somatosensory cortex," *Neuroimage* **27**, 279–290 (2005).

16. R. Graaff, J. G. Aarnoudse, J. R. Zijp, P. M. Sloot, F. F. de Mul, J. Greve, and M. H. Koelink, "Reduced light-scattering properties for mixtures of spherical particles: a simple approximation derived from Mie calculations," *Appl. Opt.* **31**, 1370–1376 (1992).

17. S. J. Matcher, M. Cope, and D. T. Delpy, "*In vivo* measurements of the wavelength dependence of tissue-scattering coefficients between 760 and 900 nm measured with time-resolved spectroscopy," *Appl. Opt.* **36**, 386–396 (1997).

18. P. Verant, R. Serduc, B. Van Der Sanden, C. Remy, and J. C. Vial, "A direct method for measuring mouse capillary cortical blood volume using multiphoton laser scanning microscopy," *J. Cereb. Blood Flow Metab.* **27**, 1072–1081 (2007).

19. A. Nimmerjahn, F. Kirchhoff, J. N. Kerr, and F. Helmchen, "Sulforhodamine 101 as a specific marker of astroglia in the neocortex *in vivo*," *Nat. Methods* **1**, 31–37 (2004).

20. Q. Fang, S. Sakadzic, L. Ruvinskaya, A. Devor, A. M. Dale, and D. A. Boas, "Oxygen advection and diffusion in a three-dimensional vascular anatomical network," *Opt. Express* **16**, 17530–17541 (2008).

21. H. H. Lipowsky, S. Usami, and S. Chien, "*In vivo* measurements of "apparent viscosity" and microvessel hematocrit in the mesentery of the cat," *Microvasc. Res.* **19**, 297–319 (1980).

22. H. H. Lipowsky, S. Usami, S. Chien, and R. N. Pittman, "Hematocrit determination in small bowel bore tubes from optical density measurements under white light illumination," *Microvasc. Res.* **20**, 51–70 (1980).

23. F. Helmchen and W. Denk, "Deep tissue two-photon microscopy," *Nat. Methods* **2**, 932–940 (2005).

24. D. Kleinfeld, P. P. Mitra, F. Helmchen, and W. Denk, "Fluctuations and stimulus-induced changes in blood flow observed in individual capillaries in layers 2 through 4 of rat neocortex," *Proc. Natl. Acad. Sci. U. S. A.* **95**, 15741–15746 (1998).

25. M. Oheim, E. Beaurepaire, E. Chaigneau, J. Mertz, and S. Charpak, "Two-photon microscopy in brain tissue: parameters influencing the imaging depth," *J. Neurosci. Methods* **111**, 29–37 (2001).

26. P. Theer and W. Denk, "On the fundamental imaging-depth limit in two-photon microscopy," *J. Opt. Soc. Am. A* **23**, 3139–3149 (2006).

27. A. K. Dunn, V. P. Wallace, M. Coleno, M. W. Berns, and B. J. Tromberg, "Influence of optical properties on two-photon fluorescence imaging in turbid samples," *Appl. Opt.* **39**, 1194–1201 (2000).

28. G. H. Spencer and M. V. R. K. Murty, "General Ray-Tracing Procedure," *J. Opt. Soc. Am.* **52**, 672–676 (1962).

29. H. H. Lipowsky, "Microvascular rheology and hemodynamics," *Microcirculation* **12**, 5–15 (2005).

30. A. Villringer, A. Them, U. Lindauer, K. Einhaupl, and U. Dirnagl, "Capillary perfusion of the rat brain cortex: an *in vivo* confocal microscopy study," *Circ. Res.* **75**, 55–62 (1994).

31. Q. Fang and D. A. Boas, "Monte Carlo simulation of photon migration in 3D turbid media accelerated by graphics processing units," *Opt. Express* **17**, 20178–20190 (2009).

32. V. Twersky, "Absorption and multiple scattering by biological suspensions," *J. Opt. Soc. Am.* **60**, 1084–1093 (1970).

33. A. Devor, S. Sakadzic, M. A. Yucel, I. C. Teng, K. A. Kasischke, and D. A. Boas, "*In vivo* functional NADH imaging with single-cell resolution," *2009 Neuroscience Meeting Planner*, Program No. 672.10/EE127 (online), Society for Neuroscience, Chicago (2009).

34. J. B. Mandeville, J. J. Marota, B. E. Kosofsky, J. R. Keltner, R. Weissleder, B. R. Rosen, and R. M. Weisskoff, "Dynamic functional imaging of relative cerebral blood volume during rat forepaw stimulation," *Magn. Reson. Med.* **39**, 615–624 (1998).

35. C. W. Shuttleworth, A. M. Brennan, and J. A. Connor, "NAD(P)H fluorescence imaging of postsynaptic neuronal activation in murine hippocampal slices," *J. Neurosci.* **23**, 3196–3208 (2003).

36. R. S. Kramer and R. D. Pearlstein, "Cerebral cortical microfluorometry at isosbestic wavelengths for correction of vascular artifact," *Science* **205**, 693–696 (1979).

37. R. S. Balaban and L. J. Mandel, "Metabolic substrate utilization by rabbit proximal tubule. An NADH fluorescence study," *Am. J. Physiol.* **254**, F407–F416 (1988).

38. M. Boldt, K. Harbig, G. Weidemann, and D. W. Lubbers, "A sensitive dual wavelength microspectrophotometer for the measurement of tissue fluorescence and reflectance," *Pflugers Arch.* **385**, 167–173 (1980).

39. K. Harbig, B. Chance, A. G. Kovach, and M. Reivich, "*In vivo* measurement of pyridine nucleotide fluorescence from cat brain cortex," *J. Appl. Physiol.* **41**, 480–488 (1976).

40. F. F. Jobsis, M. O'Connor, A. Vitale, and H. Vreman, "Intracellular redox changes in functioning cerebral cortex. I. Metabolic effects of epileptiform activity," *J. Neurophysiol.* **34**, 735–749 (1971).

41. F. F. Jobsis and W. N. Stainsby, "Oxidation of NADH during contractions of circulated mammalian skeletal muscle," *Respir. Physiol.* **4**, 292–300 (1968).

42. R. S. Bradley and M. S. Thorniley, "A review of attenuation correction techniques for tissue fluorescence," *J. R. Soc. Interface* **3**, 1–13 (2006).

43. A. P. Koretsky, L. A. Katz, and R. S. Balaban, "Determination of pyridine nucleotide fluorescence from the perfused heart using an internal standard," *Am. J. Physiol.* **253**, H856–H862 (1987).

44. M. C. Aalders, H. J. Sterenborg, F. A. Stewart, and N. van der Vange, "Photodetection with 5-Aminolevulinic acid-induced protoporphyrin IX in the rat abdominal cavity: drug-dose-dependent fluorescence kinetics," *Photochem. Photobiol.* **72**, 521–525 (2000).

45. P. Tian, A. Devor, S. Sakadzic, A. M. Dale, and D. A. Boas, "Monte Carlo simulation of the spatial resolution and depth sensitivity of two-dimensional optical imaging of the brain," *J. Biomed. Opt.* **16**, 016006 (2011).

46. H. J. Sterenborg, A. E. Saarnak, R. Frank, and M. Motamedi, "Evaluation of spectral correction techniques for fluorescence measurements on pigmented lesions *in vivo*," *J. Photochem. Photobiol. B* **35**, 159–165 (1996).

47. M. Sinaasappel and H. J. Sterenborg, "Quantification of the hematoporphyrin derivative by fluorescence measurement using dual-wavelength excitation and dual-wavelength detection," *Appl. Opt.* **32**, 541–548 (1993).